Al–N–H compounds derived from ammonia alane: Synthesis strategies and characterization

Maxence Vincent, Thibault Charpentier, Raphaël Janot, Eddy Petit, Umit B Demirci

International Journal of Hydrogen Energy 220 (2026) 154122

Contents lists available at ScienceDirect

International Journal of Hydrogen Energy

journal homepage: www.elsevier.com/locate/he

Al–N–H compounds derived from ammonia alane: Synthesis strategies and characterization

Maxence Vincent [a], Thibault Charpentier [b], Raphaël Janot [c], Eddy Petit [d], Umit B. Demirci [a,*]

[a] Institut Europeen des Membranes, IEM – UMR 5635, Univ Montpellier, ENSCM, CNRS, Montpellier, France
[b] Université Paris-Saclay, CEA, CNRS, NIMBE, 91191, Gif-sur-Yvette Cedex, France
[c] Laboratoire de Réactivité et Chimie des Solides (LRCS), CNRS UMR7314, Université de Picardie Jules Verne, 15 Rue Baudelocque, Cedex 1, 80039, Amiens, France
[d] PAC Chimie Balard, Univ Montpellier, CNRS, ENSCM, Montpellier, France

ARTICLE INFO

Keywords:
Alane-ammonia complex
Ammonia alane
Lewis acid-base reaction
Metathesis-dehydrogenation
Hydrogen carrier
Thermolysis
Hydrogen storage

ABSTRACT

Ammonia alane (AlH_3NH_3, AA) is a solid hydrogen carrier with a high gravimetric hydrogen storage capacity of 12.86 wt%. In this study, we present the first experimental investigation of Al–N–H compounds synthesized via three distinct routes: (i) Lewis acid-base reaction, (ii) metathesis, and (iii) cryo-milling. Characterization techniques including FTIR spectroscopy, thermal analysis, X-ray photoelectron spectroscopy, and solid-state ^{1}H and ^{27}Al MAS NMR spectroscopy revealed the coexistence of multiple aluminum environments. However, the successful formation of AA could not be confirmed. Ambient storage and mild thermal activation (at 80 °C) led to the formation of Al–N polymers, likely resulting from dehydrogenation and partial deammoniation, underscoring the thermal instability of these phases. These findings highlight the need for a rigorously controlled synthesis-to-characterization workflow under inert and subzero conditions (below −45 °C) to enable the isolation, comprehensive characterization, and evaluation of pristine AA for solid-state reversible hydrogen storage applications.

1. Introduction

The search for efficient chemical hydrogen storage materials is a major focus in the development of sustainable energy technologies. Two main strategies are currently being pursued: (i) physisorption, which relies on weak van der Waals interactions in porous materials such as metal-organic frameworks (MOFs) [1] or carbon-based adsorbents [2]; and (ii) chemisorption, which involves the formation of strong chemical bonds, particularly in chemical hydrides. Among these hydrides, ammonia borane (BH_3NH_3, AB, 30.87 g mol^{-1}) has emerged as a model compound. It has been extensively studied due to its high hydrogen content (19.6 wt%) and stability at room temperature under an inert atmosphere. Its decomposition follows a well-defined pathway leading to B–N polymeric species, and its structure-property relationships have been thoroughly characterized over the past two decades [3,4]. In contrast, its aluminum analog, namely ammonia alane (AlH_3NH_3, AA, 47.0 g mol^{-1}), remains underexplored, despite belonging to the same chemical family and being already reported in mid-20th century studies by Wiberg and May [5]. The lack of structural and spectroscopic data on AlH_3NH_3 prompted us to investigate this aluminum-based hydride [6]. Notably, AA has a gravimetric hydrogen density of 12.86 wt%. Like AB, it contains both hydridic and protic hydrogen, carried by the aluminum and nitrogen atoms, respectively. These atoms are connected via a dative covalent bond.

As previously mentioned, the first attempt to synthesize aminoalane (AA) dates back to the seminal work of Wiberg and May [5]. By reacting AlH_3 with NH_3 in diethyl ether (DE) at −80 °C (Fig. 1), they isolated a white precipitate identified as AA. Upon thermal treatment, this compound underwent polymerization, first forming polyaminoalane (PAA) around 20 °C, then polyiminoalane (PIA) between 20 and 100 °C, and ultimately aluminum nitride (AlN) at elevated temperatures (approximately 430 °C). They further investigated the effect of increased ammonia stoichiometry and identified intermediate species such as $AlH_2(NH_2)$ (NH_3), $AlH(NH_2)_2$, and $Al(NH_2)_3$ (Fig. 1). This foundational study elucidated the stepwise transformation of AA into AlN via ammonolysis and thermal condensation pathways.

* Corresponding author.
E-mail addresses: maxence.vincent@umontpellier.fr (M. Vincent), thibault.charpentier@cea.fr (T. Charpentier), raphael.janot@u-picardie.fr (R. Janot), eddy.petit@umontpellier.fr (E. Petit), umit.demirci@umontpellier.fr (U.B. Demirci).

https://doi.org/10.1016/j.ijhydene.2026.154122
Received 17 July 2025; Received in revised form 13 February 2026; Accepted 16 February 2026
Available online 21 February 2026

Building on this work, Ochi et al. [7] employed tetrahydrofuran (THF) as an alternative solvent and provided the first infrared spectroscopic evidence of PAA as a precursor to AlN. Subsequently, Janik and Paine [8] introduced a novel route by reacting $LiAlH_4$ with NH_4Br in diethyl ether, yielding PIA after thermal treatment at 100 °C. Their preference for DE over dimethyl ether (DME) or THF was driven by the need to minimize oxygen contamination in the final AlN product. Other studies [9–12] focused on optimizing hydrogen generation through metathesis reactions involving halogenated ammonium salts in ether-based solvents. These efforts demonstrated promising yields (e.g., 5.50 wt% H_2 for the $LiAlH_4/NH_4Cl$ system in DE), although the precise structure of the resulting polymeric phases remains poorly understood.

Despite these studies, the chemistry of AA and its polymeric dehydrogenation products remains poorly understood. Furthermore, discrepancies between expected reactivity and observed atomic arrangements such as the presence of weak hydrogen interactions beyond the van der Waals limit (approximately 2.4 Å) [6,13] may influence the stability of AA. Additional challenges arise from the spontaneous dehydrogenation of AA and related intermediates at or near room temperature. This low thermal threshold limits both storage conditions and the use of conventional characterization techniques (e.g., solid-state nuclear magnetic resonance (NMR), X-ray diffraction, vibrational spectroscopy), particularly under ambient conditions.

In this context, the present study aims to reproduce the historical synthetic routes described above, while extending them through a systematic characterization of the reaction intermediates, their structural evolution, and the transformation mechanisms as functions of both temperature and storage duration. Our ultimate goal, provided that pure AA can be successfully synthesized and safely stored, is to evaluate its true potential as a hydrogen storage material.

Although several studies have reported on the synthesis and thermal decomposition of AA and related Al–N–H systems, most have remained largely empirical, providing limited structural and mechanistic understanding. The formation pathways of intermediate species, as well as the influence of synthesis conditions on phase stability and hydrogen release behavior, are still largely unknown. In particular, the nature of aluminum coordination environments and their role in stabilizing metastable Al–N–H species remain open questions. In this work, we address this lack of knowledge by systematically comparing three synthetic strategies, namely, Lewis acid-base reaction, metathesis, and cryomilling, through comprehensive structural, spectroscopic (FTIR, ^1H, and ^{27}Al MAS NMR, and XPS), and thermal analyses. This approach allows us to clarify the relationships between synthesis route, product composition, and thermal stability, thereby providing new insights into the chemistry of Al–N–H materials and their potential for solid-state hydrogen storage.

2. Experimental

2.1. Materials and methods

The following precursors were used for the synthesis of the AA samples studied: lithium aluminum hydride ($LiAlH_4$), alane N,N-dimethylethylamine complex solution ($C_2H_5N(CH_3)_2{\cdot}AlH_3$, 0.5 M in toluene), ammonium carbonate ($(NH_4)_2CO_3$), and ammonium bromide (NH_4Br). All chemicals were purchased from Sigma-Aldrich and stored in an argon-filled glovebox (MBraun M200B; $O_2 < 10.0$ ppm, $H_2O < 0.1$ ppm). Anhydrous diethyl ether ($C_4H_{10}O$, Sigma-Aldrich) was used as the solvent for both synthesis and filtration. A pressurized ammonia cylinder (purity 99.96%, $H_2O < 400$ ppmv) was supplied by Linde. To prevent solvent exposure to air and moisture, all sampling was conducted under an argon flow using conditioned glassware. The required glassware, syringe and needle for solvent handling, and magnetic stirrer were thoroughly washed, dried at 80 °C for 4 h, placed under vacuum for at least 30 min, and finally stored under an argon atmosphere.

Synthesis by metathesis-dehydrogenation in solvent was carried out adapting the procedure described in Refs. [8,14]. In the argon-filled glovebox, lithium aluminum hydride (0.2 g, 5.3 mmol) was dissolved in 50 mL of diethyl ether within a Pyrex® three-neck round bottom flask with a magnetic stirrer. Ammonium bromide (0.51 g, 5.3 mmol), equimolar to $LiAlH_4$, was weighed separately and introduced into the reaction mixture ($LiAlH_4$/diethyl ether solution). The flask had been previously transferred to an argon-vacuum line, connected to a bubbler and immersed in an isopropanol bath kept at low temperature (−20 °C) using a cryostat (Table 1). The solution was kept under stirring at 200 rpm for 2-4 h. Then, the mixture was filtered under argon atmosphere, the solid residue rinsed with fresh solvent (2 × 10 mL). To avoid a dehydrogenation, the filtrate was not put under vacuum but directly analyzed. Sample 1 presented here was not washed, as washing does not sufficiently remove the Li_2CO_3 byproduct, which is insoluble in DE, like

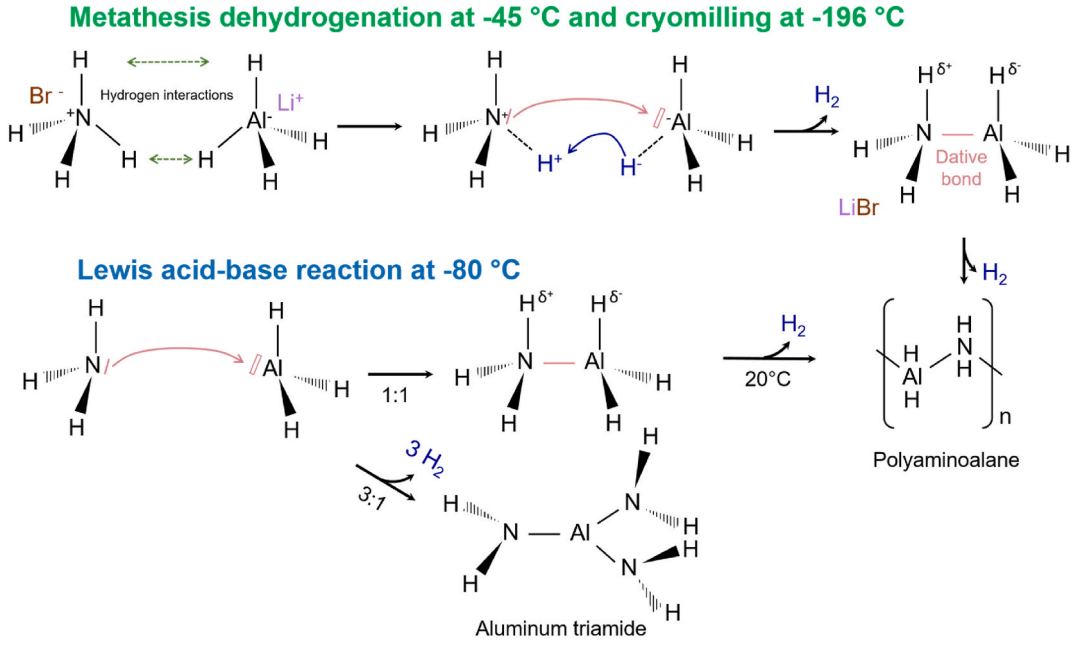

Fig. 1. Reaction toward the formation of ammonia alane.

Table 1
Reaction routes, precursors, temperature, and time, leading to AA-based compounds.

Sample name	Pathway	Precursors	Experimental conditions	Washing step[a]
M1	M/D[b]	$LiAlH_4$/$(NH_4)_2CO_3$	Magnetic stirring, −10 °C, 24h	No
M2	M/D	$LiAlH_4$/NH_4Br	Magnetic stirring, −10 °C, 24h	Yes
M3	M/D	$LiAlH_4$/NH_4Br	Magnetic stirring, 20 °C, 24h	Yes
L	L A-B[c]	AlH_3/NH_3 (l)	Magnetic stirring, −78 °C, 2h	Yes
CM	Cryo-milling	$LiAlH_4$/NH_4Br	BPR[d] 80:1, 30 Hz, −196 °C, 2 × 5 min	No

[a] *with 2 × 10 mL of DE.*
[b] M/D: Metathesis-dehydrogenation.
[c] L A-B: Lewis Acid-base reaction.
[d] Ball-to-powder ratio.

AA. By this method, 3 samples of AA, denoted **M1** to **M3**, were synthesized as reported in Table 1.

Synthesis via metathesis-dehydrogenation in solvent was carried out by adapting the procedures described in Refs. [8,14]. Inside an argon-filled glovebox, lithium aluminum hydride (0.2 g, 5.3 mmol) was dissolved in 50 mL of diethyl ether in a Pyrex® three-neck round-bottom flask equipped with a magnetic stirrer. Ammonium bromide (0.51 g, 5.3 mmol), equimolar to $LiAlH_4$, was weighed separately and added to the $LiAlH_4$/diethyl ether solution. The flask was previously transferred to an argon-vacuum line, connected to a bubbler, and immersed in an isopropanol bath maintained at −20 °C using a cryostat (Table 1). The reaction mixture was stirred at 200 rpm for 2-4 h. Filtration was performed under an argon atmosphere, and the solid residue was rinsed with fresh solvent (2 × 10 mL). To prevent dehydrogenation, the filtrate was not subjected to vacuum but analyzed directly. Sample 1 was not washed, as washing does not effectively remove the Li_2CO_3 byproduct, which is insoluble in diethyl ether, similar to AA. Using this method, three AA samples, denoted **M1** to **M3**, were synthesized, as summarized in Table 1.

Our synthesis via Lewis acid–base reaction was inspired by the work of Wiberg and May [5]. The procedure involved a double argon–vacuum ramp conducted under a fume hood. Liquefied ammonia gas was added to a cooled alane/ether mixture (−78 °C, using dry ice in a polystyrene box). An excess of ammonia was used to ensure complete reaction with alane, targeting a 1:4 alane-to-ammonia molar ratio. The resulting white precipitate was filtered, transferred to the glovebox, and washed twice with 10 mL of diethyl ether (DE). The samples were then either dried under vacuum or left undried for further analysis. As shown in Table 1, one sample, denoted as **L**, was synthesized.

Cryogenic ball milling was carried out using a RETSCH CryoMill machine, operating with liquid nitrogen (−196 °C) to maintain a cryogenic environment. Stainless steel balls with a diameter of 8 mm (2.94 g each, totaling 8.83 g) were used. The milling conditions are summarized in Table 1. Four samples produced through cryogenic ball milling were designated as **CM**. The quantity of reactants was carefully calculated to ensure that hydrogen generation did not exceed 2 bar, thereby avoiding excessive pressure buildup within the reactor.

All samples were prepared and transferred under an inert atmosphere in an argon-filled glovebox to prevent degradation due to air or moisture contamination. They were subsequently stored in a freezer at −20 °C to minimize any potential hydrogen release. Sample analysis was performed using Fourier transform infrared (FTIR) spectroscopy with attenuated total reflection (ATR) sampling, employing a Nicolet 710 spectrometer (64 scans, 4 cm^{-1} resolution).

Powder X-ray diffraction (PXRD) patterns were collected using a PANalytical X'Pert Spinner diffractometer equipped with a Cu Kα radiation source ($K_{\alpha1}$ = 1.5406 Å, $K_{\alpha2}$ = 1.5444 Å, K_{β} = 1.3922 Å), operating at 45 kV and 20 mA. Scans were performed in continuous mode over a 2θ range of 10.02° to 69.98°, with a step size of 0.033°. For samples **M3** and **CM**, a sample holder with a beryllium window was used, while the remaining samples were analyzed using a holder covered with Kapton® film.

Thermogravimetric analysis coupled with mass spectrometry (TGA-MS) was performed using a TGA/STA449F1 NETZSCH instrument under the following conditions: sample mass of 2-7 mg, 100 µL aluminum crucible, heating rate of 5 °C min^{-1}, and argon flow of 30-50 mL min^{-1}. Both instruments were calibrated within the studied temperature range (30-400 °C for TGA). The monitored mass-to-charge (*m/z*) values included 2 (H_2), 17 (NH_3), and 28 (N_2). Solvent-related fragments were identified at *m/z* 31 for diethyl ether and *m/z* 91 for toluene. Additional *m/z* signals were examined during the analysis; however, no other volatile species were detected. Some AA samples were heat-treated under vacuum at 80 °C. It is acknowledged that these compounds undergo temporal evolution, and uncertainties related to the timing of analysis may affect the resulting data.

Magic-Angle Spinning (MAS) NMR spectroscopy measurements were performed using a Varian 600 MHz spectrometer operating at a magnetic field strength of 14.09 T, corresponding to Larmor frequencies of 599.76 MHz for ^1H (spin 1/2) and 156.28 MHz for ^{27}Al (spin 5/2). The MAS frequency was set to 20 kHz, and the sample temperature was maintained at −20 °C to prevent dehydrogenation, as spinning without temperature control induces heating. Powdered samples were packed into 3.2 mm zirconia rotors inside an argon-filled glovebox. ^1H spectra were acquired using a one-pulse sequence with a recycle delay of 4 or 5 s. The L series spectra were recorded using a presaturation sequence followed by a rotor-synchronized spin-echo pulse sequence (echo delay of 2 ms), which enhances spectral resolution by suppressing contributions from strongly coupled protons (via magnetic dipolar interactions), thereby reducing broad components in the NMR spectrum. ^{27}Al spectra were acquired using a single short pulse (small flip angle) to ensure quantitative accuracy, as long radio-frequency pulses can lead to non-uniform excitation due to quadrupolar interactions. The recycle delay varied between 1 s and 4 s. Experimental data were processed and fitted using Dmfit software, applying the "czsimple" model. The deconvolutions are qualitative and intended primarily for visual guidance; satellite transitions were not included in the fitting procedure. It should be noted that liquid-state ^{27}Al NMR analysis did not yield any signal due to the poor solubility of the final products in common solvents.

X-ray photoelectron spectroscopy (XPS) analyses were conducted using a Thermo Electron ESCALAB 250 spectrometer equipped with a monochromatic Al Kα radiation source (1486.6 eV), operated at 150 W (15 kV, 10 mA). Spectra were acquired directly from powdered samples arranged on a sample holder within a high-vacuum chamber ($\leq 10^{-9}$ Torr). The analyzed area had a diameter of approximately 500 µm. Survey spectra were recorded with a step size of 1 eV at a pass energy of 150 eV, while high-resolution spectra were acquired with a step size of 0.1 eV at a pass energy of 20 eV. All binding energies were referenced to the C 1s peak of the aliphatic C–C component at 284.8 eV. The spectrometer's energy scale was calibrated using standard reference materials: Au 4f7/2 at 84.0 eV, Ag 3d5/2 at 368.2 eV, and Cu 2p3/2 at 932.6 eV. Charge compensation was applied using a low-energy electron flood gun (−2 eV). Quantification was performed based on the peak areas of the high-resolution spectra, corrected using appropriate sensitivity factors. Background signals were removed using the Shirley method [15]. Surface atomic concentrations were determined from photoelectron peak areas using the atomic sensitivity factors reported by Scofield [16]. No significant changes were observed upon repeated scans, indicating minimal beam-induced damage during data acquisition.

2.2. Experimental observations

In general, polar aprotic solvents such as DE, THF, and dioxane do not efficiently dissolve ionic salts. However, LiBr, formed in situ from

the reaction between $LiAlH_4$ and NH_4Br, exhibits sufficient solubility in DE. This justifies the use of NH_4Br and $LiAlH_4$ in this system.

The visual appearance of the powders obtained from the various synthesis routes varied noticeably. Samples **M1** and **M3** exhibited a light gray color, similar to that of $LiAlH_4$, while samples **M2** and **L** appeared white, consistent with the observations reported by Wiberg and May [5] for the latter. In contrast, sample **CM** displayed a dark gray color, even darker than the original $LiAlH_4$. These visual differences are further illustrated in the supplementary material (Fig. S1).

Manual milling of NH_4Br and $LiAlH_4$ was initially attempted for AA synthesis; however, XRD analysis revealed only the diffraction peaks of NH_4Br and $LiAlH_4$ (Fig. S2). NMR spectra further confirmed the presence of unreacted $LiAlH_4$ (Fig. S3), indicating that no reaction occurred under these conditions. Detailed experimental procedures and analytical spectra are provided in the supplementary material. To improve reaction efficiency and mitigate potential hydrogen release caused by ball impacts, cryo-milling was subsequently employed at −196 °C.

Among the three synthetic strategies explored, the Lewis acid-base route is the most effective. This method enables the formation of Al–N–H compounds without generating undesirable by-products such as LiBr or metallic aluminum, which are observed for the metathesis and cryo-milling methods. Importantly, this approach leads to the formation of an additional, less stable Al environment, highlighting its particular relevance for accessing metastable Al species that cannot be reached through the other routes. The metathesis route is easier to implement experimentally compared to the Lewis acid–base reaction and proceeds under milder conditions than cryo-milling, but very delicate solvent handling and filtration must be performed and complexation reactions can occur leading to undesired products. Finally, cryo-milling offers the simplest experimental setup since no solvent is used. This greatly minimizes exposure of the product to ambient conditions; this also aligns with the solvent-free nature of the process, preventing undesired complexation during synthesis.

2.3. Computational methodology

To investigate the Al–N bonding environment, density functional theory (DFT) calculations were performed using the B3LYP hybrid functional and the 6-311G(2d,p) basis set, as implemented in Gaussian 09. Full computational details are provided in the supplementary material. Simulations of liquid-state NMR (Fig. S4), infrared (IR) spectra (Fig. S5), and vibrational mode representations (Fig. S6) were also conducted, offering theoretical references for comparison with the experimental data.

Density functional theory (DFT) calculations yielded a total energy of −300.45 Hartree for the optimized structure, consistent with previously reported values ranging from approximately −299.2 to −301 Hartree [17–19]. During geometry optimization and molecular dynamics simulations, we observed that polyaminoalane (PAA) exhibits a pronounced tendency toward intramolecular cyclization, primarily through the formation of four-membered rings. While this behavior appears systematic under the simulated conditions for short molecular fragments, it remains uncertain whether similar cyclization tendencies occur in longer PAA chains.

The electronic distribution in AA and linear PAA was investigated by visualizing the highest occupied molecular orbital (HOMO) and the lowest unoccupied molecular orbital (LUMO), as shown in Fig. 2. The HOMO is predominantly localized over the Al–H bonds, indicating that these hydrogen atoms are electron-rich and may exhibit nucleophilic reactivity. In contrast, the LUMO is primarily centered on the NH_3 group, suggesting that this moiety could serve as the main electron acceptor during molecular interactions or reactions (Fig. 2). For PAA, the terminal aluminum atom represents the primary reactive site. Additionally, the nitrogen atoms N1 and N2 may participate in further reactions, potentially leading to molecular branching.

Mulliken charge calculations for AA revealed a partial electronic density of +0.57 on aluminum, −0.23 on its hydridic hydrogen atoms, −0.79 on nitrogen, and +0.30 on its protic hydrogen atoms. These values reflect the electronic distribution within the molecule. Notably, aluminum exhibits a lower electronegativity ($\chi = 1.61$ on the Pauling scale) compared to boron ($\chi = 2.04$), which may influence its chemical behavior and bonding characteristics.

3. Results and discussion

3.1. FTIR spectroscopy

The FTIR spectra of all samples are presented in Fig. 3. The first domain, spanning 2800-3400 cm^{-1}, corresponds to N–H stretching modes from ammonium compounds [20], consistent with the bands observed for the NH_4Br reactant (Fig. S7). N–H vibrations involved in heteropolar N–H···H–Al interactions from the direct reaction exhibit

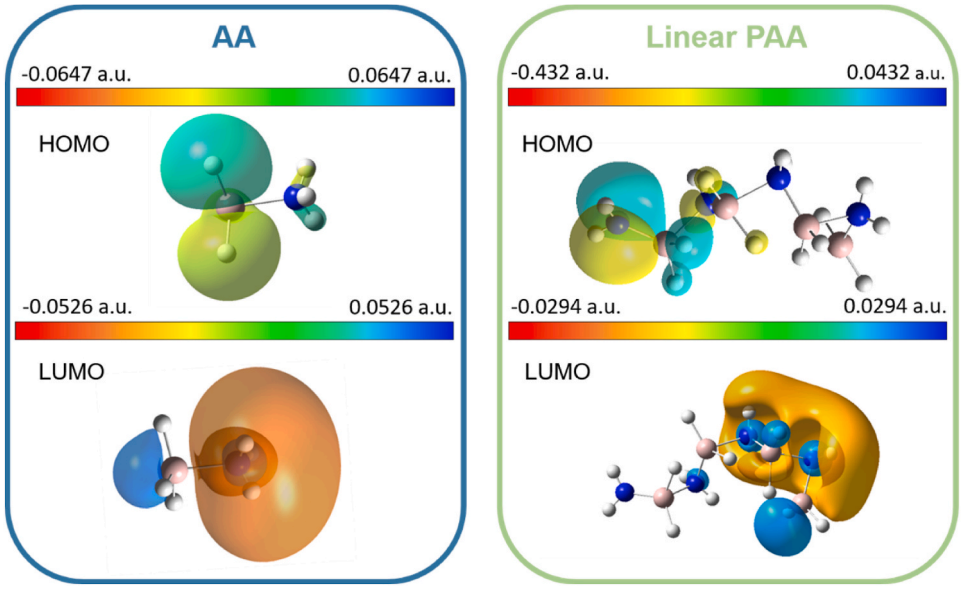

Fig. 2. Highest occupied molecular orbital (HOMO) and lowest unoccupied molecular orbital (LUMO) distributions for AA and PAA. Values are reported in atomic units (a.u.).

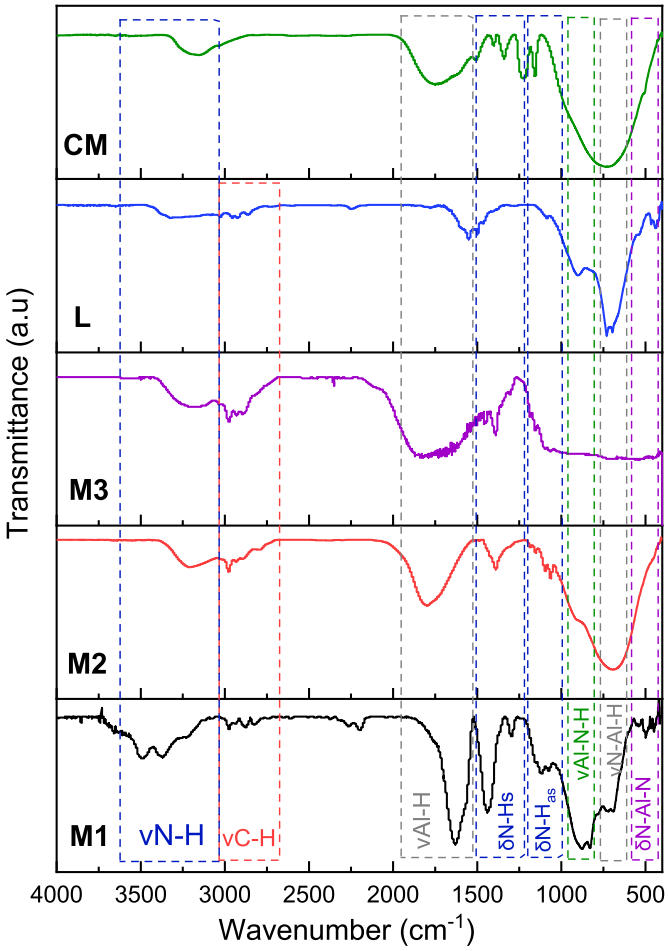

Fig. 3. FTIR spectra of the synthesized samples **M1**, **M2**, **M3**, **L** and **CM**.

higher wavenumbers, between 3000 and 3450 cm^{-1}. Diethyl ether (DE) was not used in the direct synthesis, and the cryo-milling procedure involved no solvent and remained strictly isolated from air. These observations suggest that the broad absorption band is more likely associated with N–H rather than O–H vibrations. The broad nature of this signal likely results from a highly amorphous compound that has already undergone partial polymerization, a phenomenon commonly observed in ammonia borane and its polymers formed via dehydrocoupling [4]. A decrease in the intensity of N–H stretching vibrations was observed across all samples, consistent with the spectra of related compounds reported by Uchida et al. [21]. This attenuation may be attributed either to the formation of new interactions with limited IR visibility or to a phase transition from crystalline to amorphous. The latter appears more plausible, as supported by the XRD patterns discussed below.

The Al–H bonds were identified through stretching vibrations observed in the 1600-1400 cm^{-1} region [22]. Symmetric and asymmetric N–H bending modes appeared within the 1500-1000 cm^{-1} range. The absorption band at 905 cm^{-1} was assigned to Al–N–H stretching, while the band peaking at 730 cm^{-1} was attributed to N–Al–H vibrations and rotational modes, in agreement with previous studies [7–9,23]. Despite structural transformations, the emergence of the Al–N bond, central to this study, was clearly observed in the 600-900 cm^{-1} range. The band in the 420-460 cm^{-1} range may correspond to asymmetric bending of NH_3 and AlH_3 or can be AlH_2NH_2 [7], though this assignment applies only to freshly synthesized samples.

The experimental infrared spectra were also compared with the simulated spectra of AA and PAA (Fig. S5). A good overall agreement was observed, particularly in the 500-1000 cm^{-1} region, where the main vibrational features are clearly present in the spectra of the synthesized samples.

3.2. XRD patterns

The X-ray diffraction (XRD) patterns of the samples are shown in Fig. 4. For **M1**, several diffraction peaks were observed; however, reliable phase identification could not be achieved, despite comparisons with potential candidates such as $(NH_4)_2CO_3$ or Li_2CO_3. At present, the observed peaks remain unidentified, though they are likely associated with a crystalline Al–N–H compound, possibly AA or a derivative thereof.

The X-ray diffraction patterns of **M2** and **M3** show distinct Bragg reflections corresponding to LiBr, confirming the presence of this by-product as expected from the metathesis reaction. Additionally, residual NH_4Br was detected in both samples by comparison with the reference diffraction pattern of NH_4Br (Fig. S8), suggesting incomplete reaction under the applied conditions. In contrast, the diffraction pattern of **CM** shows no detectable NH_4Br reflections, indicating a more complete reaction between the precursors. Across all samples, **M2**, **M3**, and **CM**, no diffraction peaks could be attributed to a crystalline Al–N–H compound, even after repeated washing with diethyl ether. This observation is consistent with previous findings reported by Wang et al. [9].

The XRD pattern of **L** displays features characteristic of an amorphous Al–N–H compound. Based on this observation, along with the diffraction patterns discussed previously, the results suggest that the Al–N–H compounds formed under the studied conditions are predominantly amorphous. An exception is **M1**, which may exhibit partial crystallinity due to the use of a carbonate reactant (Table 1).

3.3. TGA-MS

The thermolytic decomposition of the samples was investigated using thermogravimetric analysis (Fig. 5), with the evolved gases analyzed by mass spectrometry (Fig. S9). **M1** remained stable up to 200 °C, after which decomposition began. A release of CO_2 was observed starting at 200 °C, corroborating the presence of carbonate species such as Li_2CO_3 or $(NH_4)_2CO_3$. This was followed by the release of NH_3 above 300 °C. Due to the inability to isolate well-defined reaction products and the inconclusive nature of the analytical data, this synthetic pathway was not pursued further.

M2 began to decompose at 50 °C, as evidenced by hydrogen release

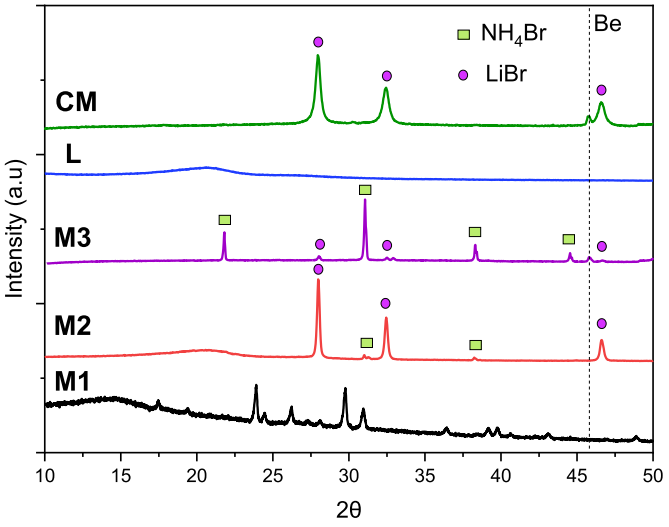

Fig. 4. XRD patterns of the synthesized samples **M1**, **M2**, **M3**, **L** and **CM**. The vertical dotted line corresponds to a reflection from the beryllium window of sample holder used for **M3** and **CM**.

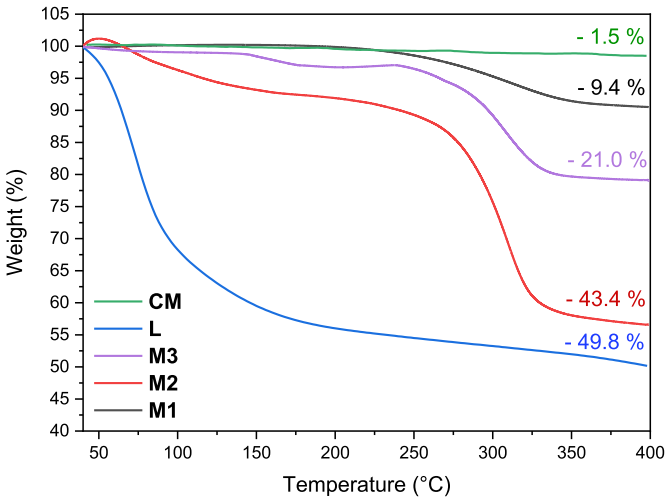

Fig. 5. TGA of the synthesized samples **M1**, **M2**, **M3**, **L** and **CM** with indication of the weight loss (in %) at 400 °C.

starting at this temperature. This corresponds to a weight loss of 8.9 wt% within the 50-150 °C range. In contrast, **M3** did not exhibit a similar hydrogen release, suggesting that part of its hydrogen content may have already been lost during synthesis and/or subsequent storage. Between 150 °C and 200 °C, both **M2** and **M3** showed a thermal plateau. At higher temperatures (200-400 °C), both samples released ammonia as the main gaseous product, along with some additional hydrogen. This resulted in a total weight loss of 34.4 wt% for **M2** and 17.9 wt% for **M3** over this temperature range.

CM exhibits a limited weight loss of approximately 1.5 wt% at 400 °C. This observation suggests two possibilities: either most of the hydrogen was released during the cryo-milling process, although no overpressure was detected in the reactor upon opening, or no hydrogen release occurs up to 400 °C, which seems unlikely for Al–N–H compounds. The synthesis of **CM** was performed under solvent-free conditions and at extremely low temperatures (−196 °C), potentially yielding highly reactive or metastable products. Under our current setup, it is not possible to maintain the sample at −196 °C after synthesis until the time of analysis. The TGA-MS instrument is located in an argon-filled glovebox, which necessitates bringing the sample to room temperature after synthesis. This temperature change may have led to partial degradation or slow hydrogen release over time. As previously mentioned, X-ray diffraction confirmed the presence of crystalline LiBr, one of the two expected reaction products, indicating that the reaction did occur. This raises the question of whether an amorphous aluminum nitride phase was also formed.

For sample **L**, a total weight loss of 49.8 wt% is observed in the 50-400 °C range. A simultaneous release of toluene and ammonia occurs at 106-107 °C, followed by hydrogen release between 60 and 200 °C. An additional hydrogen release is detected at 430 °C (Fig. S9). This hydrogen peak at 430 °C may correspond to the findings of Wiberg and May [5], who reported complete dehydrogenation at this temperature over a 4-h period.

From a broader perspective, three distinct thermal stability behaviors are observed, depending on the synthesis method used. On one hand, **M1**, **M2**, and **M3** exhibit roughly two decomposition steps: an initial step below 250 °C with varying characteristics, followed by complete decomposition above 250 °C. On the other hand, **CM** remains stable, whereas **L** shows significant decomposition, losing about half of its mass by 400 °C. These differences can be attributed to the synthesis conditions, specifically the lower temperature employed in the direct synthesis of **L** compared to the metathesis-based routes. Compounds synthesized via metathesis may have already undergone partial hydrogen release during or after synthesis, while **L** may have retained all its volatile components prior to analysis. Additionally, the presence of residual toluene in **L** might contribute to its stability, potentially through weak coordination or solvation effects (as reported for AB, for example [24]), thereby delaying hydrogen release until thermal activation. It is also worth noting that, aside from the residual solvent, **L** appears to be compositionally purer than the metathesis-derived samples, which contain residual by-products as evidenced by XRD.

3.4. MAS-NMR spectroscopy

3.4.1. ^{1}H NMR

The ^{1}H MAS NMR spectra display several distinct resonances ranging from −0.4 to 7 ppm (Fig. 6). Notably, a broad and intense signal centered at 7 ppm is attributed to ammonia molecules coordinated to

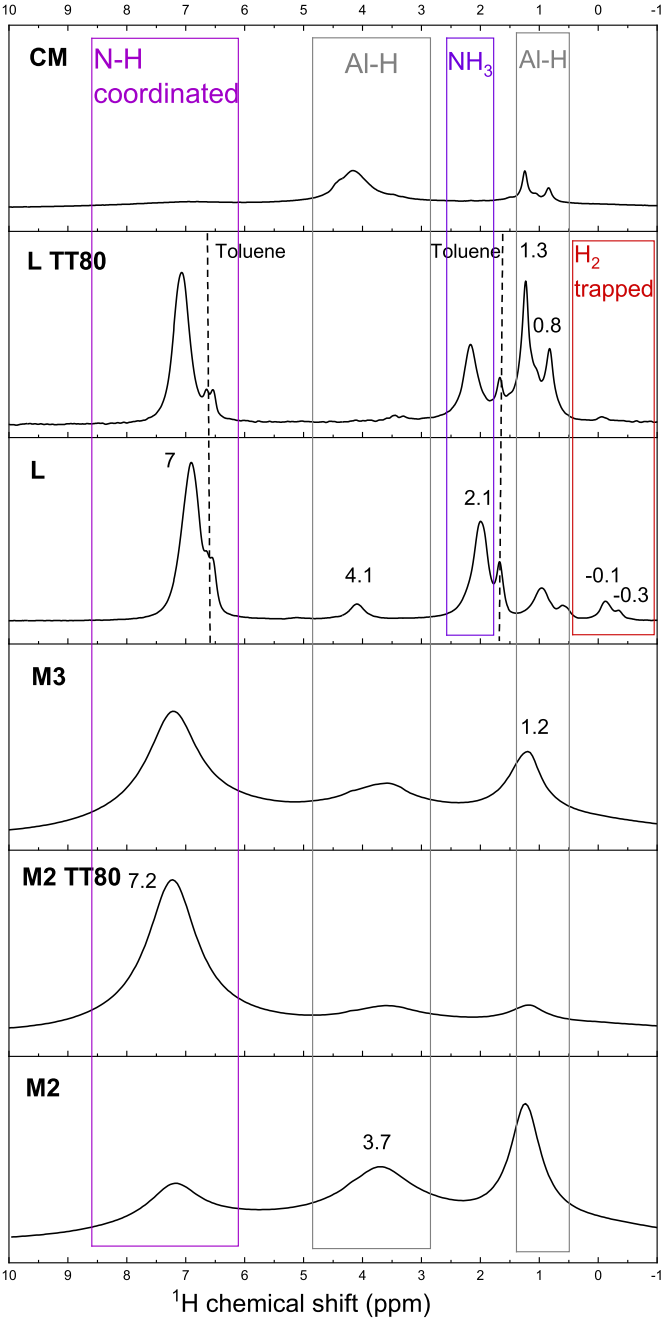

Fig. 6. ^{1}H MAS NMR spectra of samples **M1**, **M2**, **M3**, **L** and **CM**, as well as those of samples **L TT80** and **M2 TT80**. Narrow signals detected at 6.6 and 1.6 ppm are assigned to residual toluene from the synthesis **L**.

electrophilic aluminum centers, consistent with the formation of Lewis acid-base adducts such as AlH_3NH_3. A weak signal at 4.3 ppm, along with a broader component around 3.7 ppm, is assigned to Al–H species [22].

Additional resonances at 2.1, 1.3, and 0.8 ppm may correspond to weakly coordinated ammonia or hydrogen atoms within a disordered polyaminoalane-like framework. Two weak and highly shielded signals observed at −0.1 and −0.3 ppm suggest the presence of molecular H_2 trapped within amorphous domains.

A comparison of the ^{1}H MAS NMR spectra reveals significant differences between the **M** and **L** series. Based on the spectral features of **M3** (discussed in the ^{27}Al section below), a thermal treatment was applied to **M2** at 80 °C (denoted **M2 TT80**). This temperature was chosen to induce partial structural rearrangement without triggering complete gas release. The same treatment was also applied to sample **L** (denoted **L TT80**). The relative signal intensities vary across samples. In freshly prepared material such as **M2**, Al–H appears to be the dominant environment. In contrast, NH_3-type environments become predominant in **M2 TT80** and **M3**. Interestingly, sample **CM** does not exhibit any detectable NH_3-related resonance, which may explain the low mass loss observed in TGA-MS. The most plausible explanation is the premature release of NH_3 prior to or during synthesis. Finally, **L** and **L TT80** show nearly identical spectral profiles. However, the signal around 1 ppm (associated with Al–H) appears more pronounced in **L TT80**, potentially indicating a higher polymer content. Nevertheless, the non-quantitative nature of these spectra limits the depth of analysis.

3.4.2. *^{27}Al MAS-NMR*

The ^{27}Al MAS NMR spectrum of $LiAlH_4$ was recorded (Fig. S10). A characteristic resonance at 98 ppm is attributed to tetrahedral aluminum in $(AlH_4)^-$ [25], while the signal at 1634 ppm corresponds to metallic aluminum [26]. A minor resonance at −33 ppm, assigned to six-coordinate aluminum in Li_3AlH_6, was also observed. This signal likely arises from partial degradation of $LiAlH_4$ during storage [25].

Fig. 7 shows the central region (centerband) of the ^{27}Al MAS NMR spectra of the studied samples. The complex lineshape observed between 110 ppm and 10 ppm suggests the presence of multiple aluminum environments. Since ^{27}Al is a half-integer spin nucleus (I = 5/2), the central transition (−1/2 ↔ +1/2), which appears in this region, is subject to second-order quadrupolar broadening under MAS, in addition to chemical shift effects. The observed lineshapes deviate significantly from the typical second-order quadrupolar patterns seen in crystalline samples. Instead, they are consistent with the Gaussian Isotropic Model (GIM) [27,28], which reflects a broad distribution of local electric field gradient (EFG) tensors and, consequently, a wide range of coordination geometries.

Deconvolution of the spectra for **M2**, **M2 TT80**, and **M3** revealed recurring peaks at chemical shift values of 107, 96, and 70 ppm. The peak at 107 ppm is attributed to an R_3N–AlH_3 environment (where R represents aromatic or aliphatic carbon groups) [22]. The resonance at 96 ppm, although close to the typical chemical shift of $LiAlH_4$, cannot be conclusively assigned to unreacted $LiAlH_4$, as this is not supported by XRD data. An additional signal at 80 ppm suggests the formation of new species, likely associated with partial hydrogen desorption followed by the formation of polyaminoalane-type compounds, as proposed by Wiberg and May [5]. These findings support the hypothesis that the synthesis proceeded as intended, although full structural identification of the material is still pending. Nevertheless, the possibility of slight sample decomposition during synthesis, storage, or analysis cannot be entirely ruled out.

In the spectrum of sample **CM**, a dominant signal at 107 ppm and a secondary resonance at 9 ppm were observed, indicating aluminum environments more closely related to AlN-like phases than to hydrogen-rich species. This interpretation is supported by TGA results, which showed no significant mass loss, implying that the material is either thermally stable or that hydrogen release occurred during or shortly after synthesis. The unresolved resonance at 171 ppm corresponds to the outer part of the central transition associated with the main 107 ppm signal.

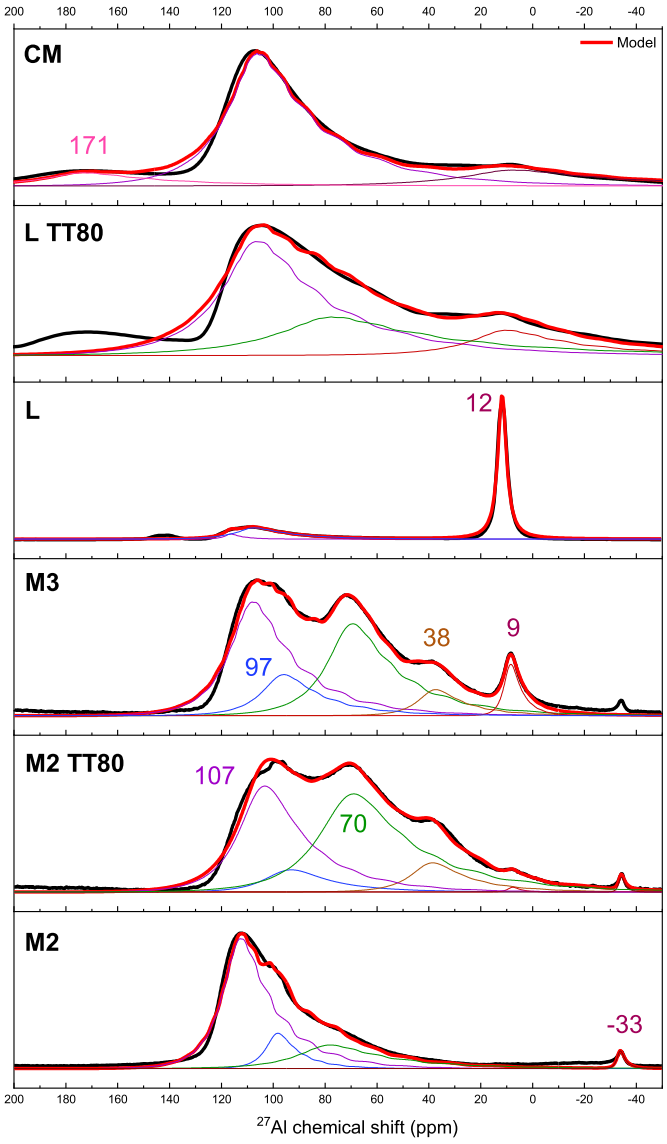

Fig. 7. ^{27}Al MAS NMR experimental spectrum (black curve) and model deconvolution (red curve), of samples **M2**, **M3**, **L** and **CM**, as well as those of samples **L TT80** and **M2 TT80**. The chemical shifts identified in these spectra are correlated with the Al–N–H compounds shown in Fig. 8. (For interpretation of the references to color in this figure legend, the reader is referred to the Web version of this article.)

A comparison of samples **M2**, **M3**, and **CM** suggests that all have undergone partial hydrogen release. The resonances initially observed at 107 ppm (purple peak) and 97 ppm (blue peak) progressively decrease in intensity with increasing temperature, indicating the gradual loss of two hydrogen-rich environments. In contrast, the signal at 70 ppm (green peak) increases in intensity, suggesting the formation of a relatively hydrogen-deficient environment. Additionally, two new resonances appear at 38 ppm and 9 ppm (ochre and brown peaks in **M2 TT80**, **M3**, and **CM**). These are tentatively attributed to hydrogen-poor species, possibly corresponding to intermediate polymeric phases such as polyaminoalane or polyiminoalane. Notably, the NMR spectrum of **M3** closely resembles that of thermally treated **M2 TT80**, indicating structural evolution during synthesis and storage, unlike the freshly synthesized **M2** sample. The presence of metallic aluminum and Li_3AlH_6

in **M2** and **M3** suggests an insufficient bromide stoichiometry to fully react with lithium ions. Cryo-milling appears to favor the formation of metallic Al due to the higher mechanical energy input. In contrast, sample L shows no metallic Al signal, highlighting the relative stability of aluminum triamide or ammonia alane species under milder synthetic conditions.

Sample **L** exhibits a low-intensity peak in the 120-100 ppm region, similar to those observed in other samples, along with a sharp resonance centered at 12 ppm. This signal can be attributed to six-coordinate species such as aluminum triamide [$Al(NH_2)_3$] or aluminum hydride-ammonia adducts [AlH_3NH_3], as proposed by Wiberg and May under similar conditions [5]. This assignment is further supported by mass spectrometry data, which show ammonia release at 106 °C. Notably, thermal treatment of sample **L** (**L TT80**) results in the near-complete disappearance of the 12 ppm signal, strongly suggesting that this environment corresponds to a labile six-coordinate adduct rather than cubic AlN. This synthesis route appears to be the most effective for producing AA or alane triamide.

In summary, the ^{27}Al MAS NMR data provide the first structural fingerprint of partially dehydrogenated and polymerized Al–N–H species, most likely derived from AA (Fig. 8). The instability of these species may be influenced by the necessity of bringing the samples to room temperature for analysis. The diversity of observed chemical shifts indicates a complex speciation landscape, comprising tetrahedral, octahedral, and potentially three-coordinate aluminum environments. Given the limited reference data available for such compounds, a more detailed structural assignment will be pursued in a forthcoming study. This will involve advanced solid-state NMR techniques, including ^{1}H–^{27}Al CPMAS, MQMAS, and 2D HETCOR experiments.

3.5. X-ray photoelectron spectroscopy

In order to have deeper insight into the chemical state of our Al–N–H samples, XPS analyses were performed on our samples. The spectra are presented in Fig. 9.

The Al 2p spectra of **M2** and **M3** exhibit multiple components that require spectral deconvolution. In both samples, the dominant contribution is centered at 74.5 eV, characteristic of Al–O environments, and is attributed to aluminum oxide, along with a contribution from metallic aluminum (Al_2O_3/Al), consistent with the NMR data (Fig. S11) [29]. The presence of aluminum oxide suggests partial surface oxidation, likely resulting from brief exposure to air during sample handling and transport. Although samples were handled under an inert atmosphere as much as possible, minor atmospheric contamination during transfer may have led to superficial oxidation. This interpretation aligns with previous findings by Parkhomenko et al. [30], who showed that oxygen incorporation in AlN thin films predominantly occurs at the surface. A secondary component at 73.9 eV is observed, which is close to binding energies reported for AlN-type environments [29,31–33]. In contrast, the **CM** sample shows a much weaker Al 2p signal at 74.5 eV, suggesting a lower surface concentration of aluminum species.

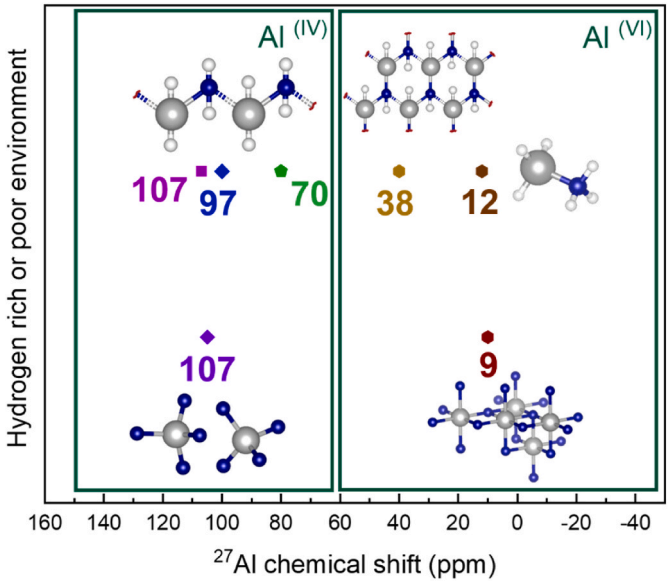

Fig. 8. Experimental ^{27}Al MAS NMR chemical shifts of the observed Al–N–H compounds, tentatively assigned to the predominant species potentially derived from AA. The identification of these species remains hypothetical and requires further experimental confirmation to validate their structural nature.

The Br 3d spectra of **M2**, **M3**, and **CM** reveal two distinct components in each sample. The main contribution, centered at 69.0 eV, is attributed to residual LiBr. A secondary peak at 68.0 eV may correspond to NH_4Br, further supporting the interpretation of incomplete reaction under the conditions employed.

The corresponding N 1s spectra reinforce these interpretations. In **M2**, a small peak at 397.6 eV is attributed to Al–N species, while a more intense contribution centered at 399.8 eV is assigned to physisorbed or coordinated NH_3 molecules. The N 1s spectrum of **M3** shows a poor signal-to-noise ratio, making reliable deconvolution difficult. This may reflect the absence of nitrogen species or the complete degradation of surface nitrogen functionalities, possibly due to extensive oxidation. In **CM**, the NH_3-related signal is less pronounced, indicating a reduced ammonia content. Intriguingly, the N 1s region of **CM** displays a dominant peak at 401.5 eV, attributed to NH_4Br or potentially other unidentified nitrogen-containing species. The detection of NH_4Br in this sample is particularly unexpected, as no corresponding signal is observed in **M2** or **M3**. Furthermore, XRD analysis does not reveal the presence of crystalline NH_4Br.

In the **L** samples, the Al 2p region shows a dominant peak centered at 73.9 eV, characteristic of Al–N coordination [29,31–33], along with a higher binding energy component at 75.0 eV corresponding to Al_2O_3 [29]. Upon thermal treatment at 80 °C, the Al–N signal in **L TT80** increases in intensity, suggesting that mild dehydrogenation enhances Al–N coordination. Deconvolution of the N 1s region reveals two components: a peak at 399.9 eV, attributed to physisorbed or weakly bound NH_3, and a dominant signal at 397.4 eV, assigned to nitrogen atoms incorporated into an AlN-like framework. These results support the hypothesis of progressive dehydrogenation upon mild heating. Furthermore, the aged **L TT80** sample (denoted **L TT80 old**) displays significantly reduced Al 2p and N 1s signal intensities, indicating nitrogen loss and highlighting the material's limited stability over time under ambient conditions.

In summary, the surfaces of the **M2**, **M3**, and **L** samples retain a chemical signature consistent with Al–N bonding. In contrast, the **CM** sample appears to be oxidized, with negligible surface concentrations of aluminum and nitrogen. These findings underscore the poor stability of Al–N–H compounds and highlight the critical influence of synthetic parameters and storage conditions on preserving their surface chemical composition. The formation and preservation of AA are highly sensitive to temperature throughout the entire workflow, from synthesis and glovebox transfer to storage and characterization. Even brief exposure to ambient conditions can trigger partial dehydrogenation or structural evolution. Therefore, to preserve the as-synthesized environments, particularly those rich in hydrogen, stringent temperature control is essential. This necessitates the development of an integrated, inert-atmosphere experimental workflow encompassing synthesis through to storage. In practice, such a strategy would require maintaining all critical steps below −45 °C, in line with the thermal stability threshold reported by Wiberg and May [5], who identified this temperature as critical for inhibiting AA decomposition.

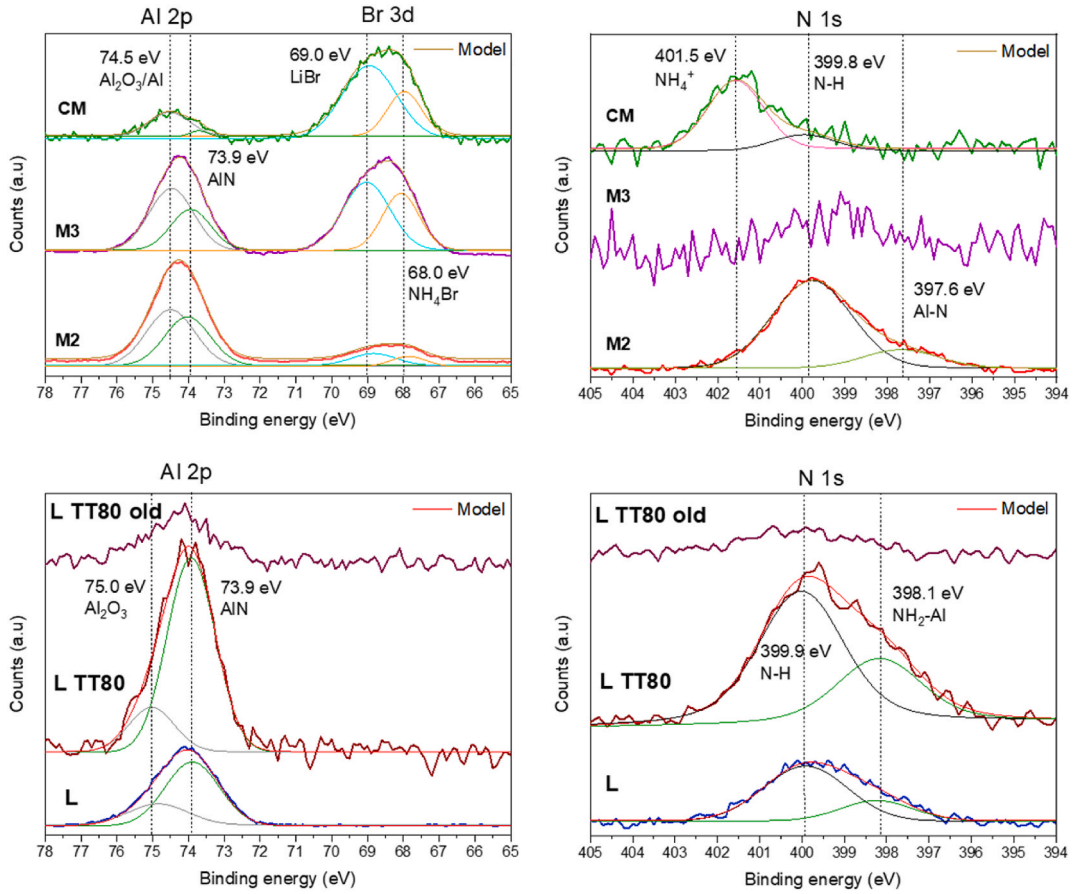

Fig. 9. N 1s and Al 2p XPS spectra of samples **M2**, **M3**, **L** and **CM**.

4. Conclusion

This study presents a comprehensive experimental investigation of ammonia alane-based compounds synthesized via three distinct routes (Lewis acid-base reaction, metathesis, and cryo-milling). These synthetic approaches reveal clear differences in their practicality and efficiency for preparing Al–N–H compounds. The metathesis route appears intrinsically limited by the low reactivity of the solid precursors, suggesting that higher activation energy or nanosized precursors would be necessary to drive the reaction to completion. Additionally, this method involves a filtration step at room temperature, raising concerns about the potential evolution of unstable species during liquid-solid separation. The cryo-milling approach addresses some of these limitations by enhancing precursor reactivity through repeated mechanical stress and avoiding solvent-mediated reaction. However, the formation of the LiBr by-product that is not removable under solvent-free conditions, significantly limits the effectiveness of the method. Moreover, even under cryogenic conditions, the mechanical energy input appears excessive, promoting the formation of metallic aluminum rather than the desired Al–N–H phase. Among the three strategies, the Lewis acid-base reaction emerges as the most reliable and reproducible route. It offers rapid reaction kinetics, a controlled chemical environment, and avoids the formation of undesired by-products. Provided the entire process is conducted below −45 °C, this method appears to be the most promising pathway for producing Al–N–H materials.

Solid-state ^{1}H and ^{27}Al MAS NMR spectroscopy confirm the coexistence of various aluminum environments, including Al–N coordination and residual metallic aluminum. Thermal activation at 80 °C promotes the formation of a polymeric phase, likely responsible for enhanced Al–N bonding, consistent with progressive hydrogen or ammonia release. In contrast, prolonged ambient storage leads to a significant loss of nitrogen functionalities and aluminum signals, underscoring the intrinsic instability of these compounds. Collectively, these findings confirm the instability of AA, which remains elusive in isolated form, as well as the susceptibility of related Al–N–H phases to thermal and environmental degradation. Future fundamental work is planned, employing advanced 2D solid-state NMR techniques, including ^{27}Al multiple quantum MAS (MQMAS), ^{1}H–^{27}Al heteronuclear correlation (HETCOR), and cross-polarization MAS (CPMAS), to further elucidate the transient coordination environments and degradation pathways. These insights will be critical for the rational design of stabilized Al–N–H compounds for reversible hydrogen storage applications.

Given the thermal sensitivity of AA, experimental infrastructure must be specifically adapted to its poor stability. This includes maintaining subzero temperatures throughout all critical stages, from synthesis and glovebox transfer to storage and characterizations.

CRediT authorship contribution statement

Maxence Vincent: Writing – original draft, Methodology, Investigation. **Thibault Charpentier:** Writing – review & editing, Methodology, Formal analysis, Data curation. **Raphaël Janot:** Writing – review & editing, Supervision, Methodology, Formal analysis. **Eddy Petit:** Writing – review & editing, Investigation, Formal analysis, Data curation. **Umit B. Demirci:** Writing – review & editing, Writing – original draft, Visualization, Validation, Supervision, Resources, Project administration, Methodology, Funding acquisition, Conceptualization.

Declaration of generative AI and AI-assisted technologies in the writing process

During the revision of this work, U. B. Demirci used Microsoft Copilot

to improve the language and correct spelling, typographical errors, and grammar. After using this tool, all authors reviewed and edited the content as needed and take full responsibility for the final publication.

Declaration of competing interest

The authors declare that they have no known competing financial interests or personal relationships that could have appeared to influence the work reported in this paper.

Acknowledgments

This work was supported by the Agence Nationale de la Recherche (ANR) under France 2030 and bearing the reference ANR-22-PEHY-0007. The authors gratefully acknowledge Emmanuel Fernandez (ENSCM, UAR PAC Chimie Balard Montpellier), Hanyu Hu (Université Paris-Saclay, CEA, CNRS, NIMBE) and Matthias Jollain (LRCS, CNRS, Université de Picardie Jules Verne, Amiens) for their contributions to the MAS NMR and TGA-MS analyses on some selected samples.

Appendix A. Supplementary data

Supplementary data to this article can be found online at https://doi.org/10.1016/j.ijhydene.2026.154122.

References

[1] Ahmed A, Liu Y, Purewal J, Tran LD, Wong-Foy AG, Veenstra M, Matzger AJ, Siegel DJ. Balancing gravimetric and volumetric hydrogen density in MOFs. Energy Environ Sci 2017;10:2459–71. https://doi.org/10.1039/C7EE02477K.

[2] Klechikov AG, Mercier G, Merino P, Blanco S, Merino C, Talyzin AV. Hydrogen storage in bulk graphene-related materials. Microporous Mesoporous Mater 2015;210:46–51. https://doi.org/10.1016/j.micromeso.2015.02.017.

[3] Frueh S, Kellet R, Mallery C, Molter W, Willis WS, King'ondu C, Suib SL. Pyrolitic decomposition of ammonia borane to boron nitride. Inorg Chem 2011;50:783–92. https://doi.org/10.1021/ic101020k.

[4] Castilla-Martinez C, Gaveau P, Semsarilar M, Alonso B, Demirci UB. Isothermal dehydrogenation of ammonia borane: insights into BNH polymers and challenges in regeneration. Chem Asian J 2025;20:11. https://doi.org/10.1002/asia.202500140.

[5] Wiberg E, May A. Notizen: über die umsetzung von aluminiumwasserstoff mit ammoniak und aminen. I. Versuche zur darstellung eines borazol-homologen "alazols" $Al_3N_3H_6$. Z Naturforsch B Chem Sci 1955;10:229–30. https://doi.org/10.1515/znb-1955-0409.

[6] Vincent M, Castilla-Martinez CA, Janot R, Demirci UB. Exploring the potential of ammonia alane AlH_3NH_3 as hydrogen carrier. Int J Hydrogen Energy 2024;74:101–11. https://doi.org/10.1016/j.ijhydene.2024.06.116.

[7] Ochi A, Kent Bowen H, Rhine WE. The synthesis of aluminum nitride from aluminum hydride. Mater Res Soc Symp Proc 1988;121:663–6. https://doi.org/10.1557/PROC-121-663.

[8] Janik JF, Paine RT. The systems $LiAlH_4/NH_4X$ and N_2H_5Cl as precursor sources for AlN. J Organomet Chem 1993;449:39–44. https://doi.org/10.1016/0022-328X(93)80104-J.

[9] Wang X, Wu C, Zhang Y, Chen Y. Hydrogen generation behaviors of $LiAlH_4$ and NH_4Cl in Et_2O, THF or DME. Int J Hydrogen Energy 2016;41:6825–32. https://doi.org/10.1016/j.ijhydene.2016.03.081.

[10] Zhang H, Loo YS, Geerlings H, Lin J, Chin WS. Hydrogen production from solid reactions between $MAlH_4$ and NH_4Cl. Int J Hydrogen Energy 2010;356:176–80. https://doi.org/10.1016/j.ijhydene.2009.10.070.

[11] Zheng X, Zheng J, Ma Q, Liu S, Feng X, Lin X, Guo X. Study on dehydrogenation properties of the $LiAlH_4$-NH_4Cl system. J Alloys Compd 2013;551:508–11. https://doi.org/10.1016/j.jallcom.2012.11.051.

[12] Wang X, Chen Y, Kong Q, Feng W, Li Z, Wu Y, Liu Y, et al. Low-temperature hydrogen release through $LiAlH_4$ and NH_4F react in Et_2O. Int J Hydrogen Energy 2020;45:8774–82. https://doi.org/10.1016/j.ijhydene.2020.01.102.

[13] Czerw M, Goldman AS, Krogh-Jespersen K. Addition of ammonia to AlH_3 and BH_3. Why does only aluminum form 2:1 adducts? Inorg Chem 2000;39:363–9. https://doi.org/10.1021/ic990961i.

[14] Petit JF, Miele P, Demirci UB. Ammonia borane H_3N-BH_3 for solid-state chemical hydrogen storage: different samples with different thermal behaviors. Int J Hydrogen Energy 2016;41:15462–70. https://doi.org/10.1016/j.ijhydene.2016.06.097.

[15] Shirley DA. High-resolution X-Ray photoemission spectrum of the valence bands of gold. Phys Rev B Condens Matter 1972;5:4709. https://doi.org/10.1103/PhysRevB.5.4709.

[16] Scofield JH. Hartree-slater subshell photoionization cross-sections at 1254 and 1487 eV. J Electron Spectrosc Relat Phenom 1976;8:129. https://doi.org/10.1016/0368-2048(76)80015-1.

[17] Davy RD, Jaffrey KL. Aluminium-nitrogen multiple bonds in small AlNH molecules: structures and vibrational frequencies of $AlNH_2$, $AlNH_3$ and $AlNH_4$. J Phys Chem 1994;98:8930–6. https://doi.org/10.1021/j100087a019.

[18] Marsh CMB, Hamilton TP, Xie Y, Schaefer HF. Ammonia alane. J Chem Phys 1992;96:5310–7. https://doi.org/10.1063/1.462716.

[19] Leboeuf M, Russo N, Salahub DR, Toscano M. A density functional study of borane and alane monoaamoniate (BH_3NH_3, AlH_3NH_3). J Chem Phys 1995;103:7408–13. https://doi.org/10.1063/1.470312.

[20] Reed JW, Williams Q. An infrared spectroscopic study of NH_4Br-ammonium bromide to 55 GPa. Solid State Commun 2006;140:202–7. https://doi.org/10.1016/j.ssc.2006.07.036.

[21] Uchida M, Takei T, Kumada N, Tsutsui H, Azuma K, Toyama T. Low temperature synthesis of aluminum nitride from anhydrous aluminum chloride-organic amine complex. JCS Japan 2022;130:707–14. https://doi.org/10.2109/jcersj2.22041. I.

[22] Humphries TD, Munroe KT, Decken A, McGrady GS. Lewis base complexes of AlH_3: prediction of preferred structure and stoichiometry. Dalton trans 2013;42:6965–78. https://doi.org/10.1039/c3dt00047h.

[23] Interrante LV, Lee W, McConnell M, Lewis N, Hall EJ. Preparation and properties of aluminum nitride films using an organometallic precursor. Electrochem Soc 1989;136:472. https://doi.org/10.1149/1.2096657.

[24] Ingram DJ, Headen TF, Skipper NT, Callear SK, Billing M, Sella A. Dihydrogen vs. hydrogen bonding in the solvation of ammonia borane by tetrahydrofuran and liquid ammonia. Phys Chem Chem Phys 2018;20:12200–9. https://doi.org/10.1039/C7CP08220G.

[25] Wiench JW, Balema VP, Pecharsky VK, Pruski M. Solid-state ^{27}Al NMR investigation of thermal decomposition of $LiAlH_4$. J Solid State Chem 2004;177:648–53. https://doi.org/10.1016/j.jssc.2003.08.006.

[26] Tarasov VP, Kirakosyan GA. Aluminohydrides: structures, NMR, solid-state reactions. Russ J Inorg Chem 2008;53:2048–81. https://doi.org/10.1134/S0036023608130044.

[27] Czjzek G, Fink J, Götz F, Schmidt H, Coey JMD, Rebouillat JP, Liénard A. Atomic coordination and the distribution of electric field gradients in amorphous solids. Phys Rev 1981;23:2513. https://doi.org/10.1103/PhysRevB.23.2513.

[28] d'Espinose de Lacaillerie JB, Fretigny C, Massiot D. MAS NMR spectra of quadrupolar nuclei in disordered solids: the czjzek model. J Magn Reson 2008;192:244–51. https://doi.org/10.1016/j.jmr.2008.03.001.

[29] Dong L, Jiang H, Zhao X, Zhang W. Influences of hydrogen ions doping on the lattice structure of AlN thin films for temperature interpretation application. Vacuum 2024;221:112901. https://doi.org/10.1016/j.vacuum.2023.112901.

[30] Parkhomenko RG, De Luca O, Kołodziejczyk Ł, Modin E, Rudolf P, Martínez Martínez D, Cunha L, Knez M. Amorphous AlN films grown by ALD from trimethylaluminum and monomethylhydrazine. Dalton Trans 2021;50:15062–70. https://doi.org/10.1039/D1DT02529E.

[31] Sharma N, Ilango S, Dash S, Tyagi AK. X-ray photoelectron spectroscopy studies on AlN thin films grown by ion beam sputtering in reactive assistance of N+/N2+ ions: substrate temperature induced compositional variations. Thin Solid Films 2017;636:626–33. https://doi.org/10.1016/j.tsf.2017.07.006.

[32] Naumkin AV, Kraut-Vass A, Gaarenstroom SW, Powell CJ. National institute of standards and technology (NIST), X-ray photoelectron spectroscopy database, version 5.0. https://srdata.nist.gov/xps/; 2023. i.

[33] Motamedi P, Cadien K. XPS analysis of AlN thin films deposited by plasma enhanced atomic layer deposition. Appl Surf Sci 2014;315:104–9. https://doi.org/10.1016/j.apsusc.2014.07.105.